Earth pressure distribution on laterally loaded offshore monopiles

Yibo Ma, Jun Yang [*]

Department of Civil Engineering, The University of Hong Kong, Pokfulam, Hong Kong, China

ARTICLE INFO

ABSTRACT

Unlike conventional pile foundations, a monopile is a large diameter open-ended steel tube driven into the seabed. Accurate quantification of the earth pressure distribution along a monopile due to lateral loads plays a pivotal role in the design of offshore wind turbines and remains a problem of great interest. This paper presents an attempt to address the problem by means of three-dimensional (3D) finite element modeling, with focus on the effect of pile slenderness on earth pressure distribution and the associated soil deformation mechanisms. The study shows that as pile diameter increases, the deformation mode of the pile will change from flexural to rotational deflection while the deformation pattern of the surrounding soil varies from being the wedge-type to a combination of the wedge-type and the rotation-type. The magnitude of either normal contact stress or shear stress at a pile section decreases with increasing pile diameter, but the distribution pattern of the normalized contact stress (either normal or shear stress) is nearly the same. The implications of these findings for engineering practice are two-fold: (a) Use of the p-y relationship established from field tests on piles of reduced scales in the design of large-diameter piles may still result in a potential risk of overestimating the lateral bearing capacity if the test pile diameter is not large; and (b) a unified factor independent of pile diameter can be introduced to average the contact stress across the pile section in the development of simplified methods.

1. Introduction

To combat climate change and to fulfill the transformation from a fossil-fuel-dominated society to a carbon-neutral one, the development and utilization of various renewable resources, such as solar, tidal, and wind energy, has become a matter of national interest in many countries around the world. Wind power, particularly, has received growing attention and investments in the last decades due to several advantages (Leung and Yang, 2012). Owing to the exhaustion of land resources for onshore wind turbines, offshore wind turbines are emerging as the major contributor of the newly installed wind power (Breton and Moe, 2009). A modern offshore wind turbine is a very tall and flexible structure installed into the seabed and subjected to the complex ocean environments, making its design and operation a challenge to researchers and engineers. A safe and cost-effective design of the foundation for the offshore wind turbine is of particular importance, for which the bearing capacity against the lateral loads from winds, waves, and currents needs to be accurately estimated and the foundation deflection needs to be carefully controlled within the strict criteria.

Among the various foundation types for offshore wind turbines, the large-diameter steel open-ended monopile is the most preferred one,

representing about 80% of all installed offshore foundations in Europe in 2020 (Wind Europe, 2021). The diameter (D) and the embedded depth (L) of a typical offshore monopile are in the ranges of 4–8 m and 25–40 m, respectively, and the corresponding aspect ratio (L/D) is in the range of 3–8 (Cao et al., 2021; Murphy et al., 2018; Wang et al., 2020a, 2021). With the increase in pile diameter for the same embedded depth, the aspect ratio of the pile decreases, and its deformation mode under lateral loading may change from flexural deformation to rotational deformation, as shown in Fig. 1. It is thus necessary to investigate in detail the pile slenderness effect on the mechanism of soil deformation and the associated earth pressure distribution.

Traditionally, in the design of a laterally loaded pile used for offshore oil and gas platforms, the p-y method, recommended by the API standard (API, 2007) and the DNV standard (Det Norske Veritas, 2011), is adopted. The method is to assume the pile-soil interaction is equivalent to an elastic beam supported by a set of uncoupled, nonlinear, soil springs. The derivation of this method was based on field tests of small-diameter piles with the diameter of 0.61 m and the aspect ratio of 34.4 (O'Neill and Murchison, 1983; Reese et al., 1974). The applicability of this original p-y model to large-diameter monopiles is a critical concern because of the distinct deformation modes of the rigid and
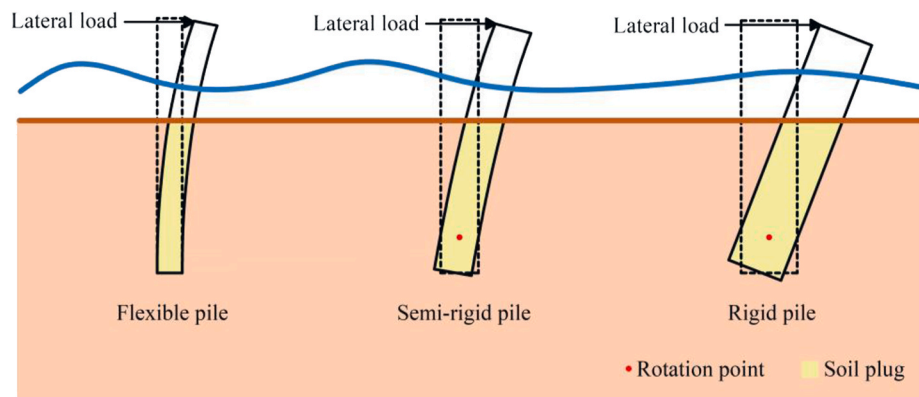
Fig. 1. Deformation modes of laterally loaded piles of different stiffness.
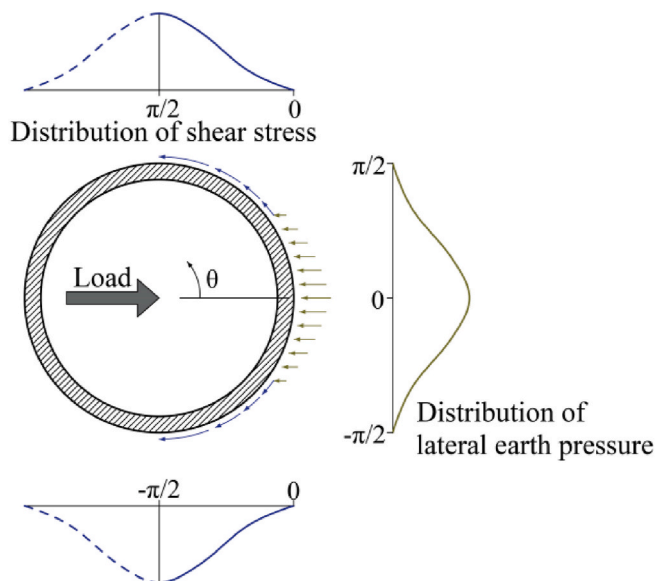

Fig. 2. Theoretical stress distributions around a laterally loaded pile (Baguelin et al., 1977; Smith, 1987).

flexible piles (LeBlanc et al., 2010; Lesny and Wiemann, 2006; Li et al., 2017; Sun et al., 2020).

To overcome the potential risk with the original p-y method for the design of large-diameter monopiles, several new p-y models incorporating additional soil resistance were proposed to consider the characteristics of the rotational deformation of monopiles. For example, a four-spring model consisting of distributed lateral resistance, distributed moment, base horizontal force and base moment was proposed by Burd et al. (2020) and Byrne et al. (2020a) for piles in sand and clay, respectively; a two-spring model consisting of distributed lateral resistance and base horizontal force was presented by Zhang and Andersen (2019) for piles in clay; and a two-spring model consisting of distributed lateral resistance above the rotation point and the moment at the rotation point was put forward by Wang et al. (2020b) for soft clay.

It should be noted that the new p-y models are mainly based on reduced-scale field test piles with low L/D ratios but small diameters due to the cost constraints, such as the field test with L/D = 3–10 and D = 0.273–2.0 m at Dunkirk and Cowden in the PISA project (Byrne et al., 2020b; McAdam et al., 2020), the field test with L/D = 4.5–9 and D = 0.61–1.22 m at Daggett (Bhushan et al., 1981), and the field test pile with L/D = 6.5 and D = 0.5 m at Blessington (Li et al., 2017). Compared with the actual offshore monopiles with the diameter of 4–8 m, these test piles (0.273–2.0m) are much smaller. In this connection, a critical

concern arises - whether the distribution of earth pressure and consequently the lateral resistance will change with a significant increase of pile diameter. Moreover, most of the previous studies focused mainly on the deflection and moment of the laterally loaded pile itself in deriving the pile-soil interaction models (Hu et al., 2021; Li et al., 2017; Luo et al., 2020; Murphy et al., 2018; Taborda et al., 2020), with little attention on the earth pressure distributions along the pile and across the pile perimeter. In the preliminary design phase, the theoretical stress distribution on the pile-soil interface proposed by Baguelin et al. (1977), as shown in Fig. 2, is usually adopted to predict the ultimate soil resistance for a laterally loaded pile (Chen et al., 2021; Sun et al., 2020; Zhang et al., 2005). However, the rationality of this theoretical model is questionable because it was established based on the assumption that the soil adheres perfectly to the pile. In real situations a gap may occur in the rear part of the pile due to lateral loading and relative slip may also take place between the pile and the soil. Based on the Coulomb's law, the shear stress at $\theta = 90°$ should be small rather than the maximum since the normal contact stress is small at this position.

Against the above background, the primary objective of this study is to address the following concerns by means of three-dimensional finite element models: (1) the pile slenderness effect on soil deformation and the associated earth pressure distribution; (2) the applicability of the earth pressure distribution and the lateral resistance derived from reduced-scale field tests to actual large-diameter offshore monopiles; and (3) the rationality of the widely-accepted theoretical stress distribution for laterally loaded piles. Three pile diameters (2 m, 5 m and 10 m) are considered, which represent respectively the cases of flexible pile, semi-rigid pile, and rigid pile for a typical pile embedment of 25 m. Besides the earth pressure distribution and soil deformation mechanism, the suitability of the current p-y models recommended by API is also evaluated for this wide range of pile diameters.

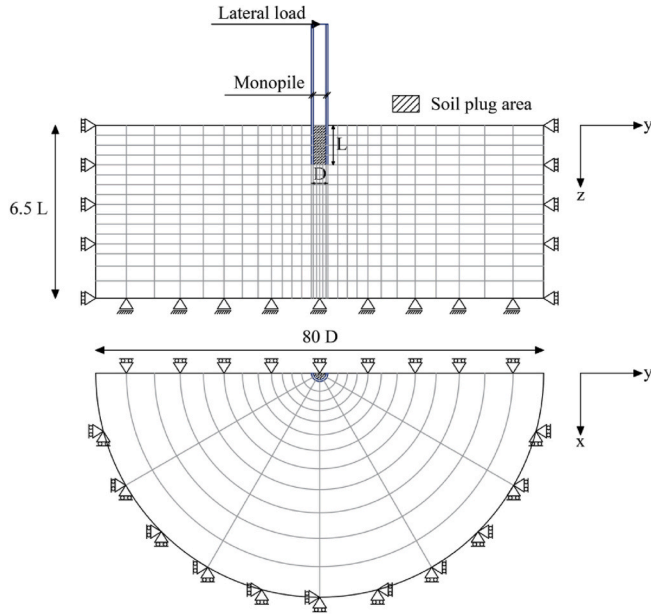## 2. Validation of 3D finite element model

Before applying the 3D finite element model to analyze the pile slenderness effect on the distribution of earth pressure and on the p-y relations for laterally loaded piles in sand, the reliability of the 3D model is carefully examined using the well-designed field tests of the PISA project (McAdam et al., 2020).
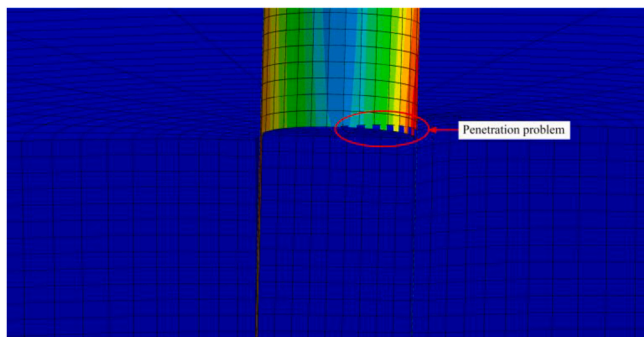
2.1. Field tests at Dunkirk

In the field tests, 12 steel hollow monopiles with the pile diameter ranging from 0.273 m to 2.0 m and the aspect ratio ranging from 3 to 10 were loaded laterally by a concentrated force at a height, *h*, above the ground from a reaction pile at Dunkirk, in northern France. The soil profile at this site is comprised of a dense hydraulically placed sand at the top 3m, underlying by dense Flandrian sand. Considering the
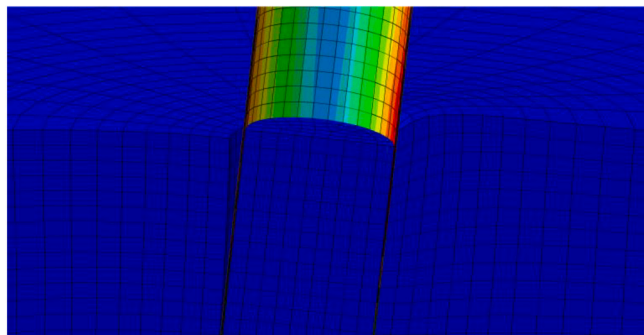
Table 1
Test pile geometries at Dunkirk.

Pile	Diameter (D: m)	Embedded depth (L: m)	Wall thickness (t: mm)	Load eccentricity (h: m)
DS1	0.273	1.43	7	5.0
DM7	0.762	2.3	10	10.0

Table 2
Parameters for the dense sand in FE models.

Parameter	Value
Unit weight, γ_s (kN/m^3)	17.1
Young's modulus, E (MPa)	90
Poisson's ratio, ν	0.17
Friction angle, φ (deg)	42
Dilatancy angle, ψ (deg)	30
Cohesion, c (kPa)	0.1
Earth pressure coefficient, K_0	0.4

Fig. 3. Schematic of the 3D FE model: cross section (top) and plan view (bottom).

(a)

(b)

Fig. 4. Discretizing the pile by different elements: (a) shell element; (b) solid element.
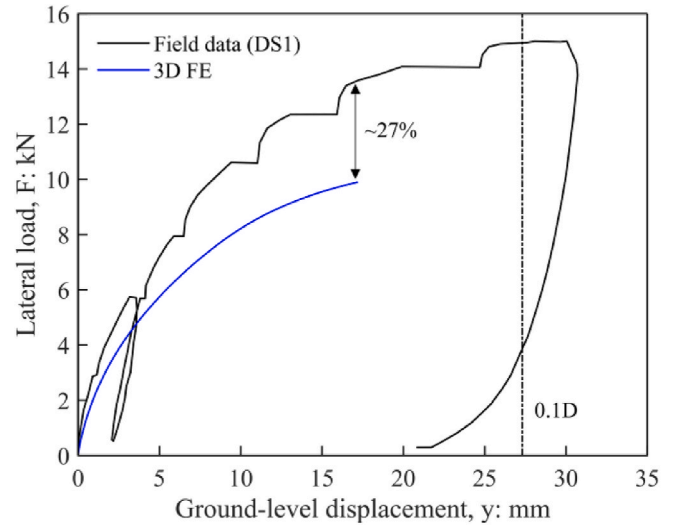
(a)
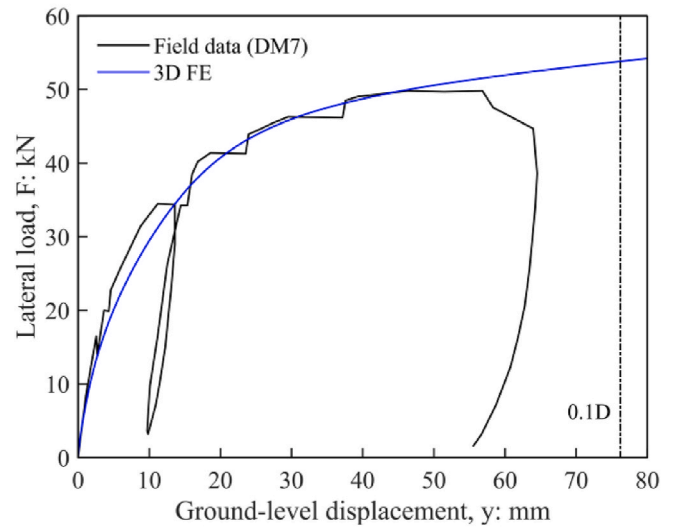
(b)

Fig. 5. Lateral load-displacement responses of two test piles: (a) pile DS1; (b) pile DM7.

homogeneity of the soil layer and assuming 10%D mudline displacement as the criterion for the ultimate limit state of a laterally loaded monopile (Cuéllar, 2011; Luo et al., 2020; Taborda et al., 2020; Zhu et al., 2015), the field test results for pile DS1 and pile DM7 are chosen here as the benchmark for the validation of the 3D FE model. The embedded depths of these two piles are within the upper dense hydraulically placed sand (3m). The detailed information of the two piles is given in Table 1. The relative density and the initial void ratio of the
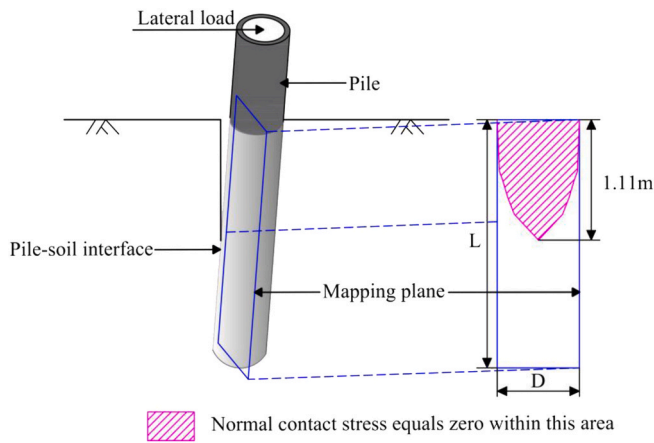
Fig. 6. Schematic illustration of the gap generated in the FE model of pile DM7.

Table 3
Geometric information of three representative piles in FE models.

Pile type	Pile geometry	$S = E_p I_p / E_s L^4$	Load eccentricity ratio
Flexible pile	D = 2 m, L = 25 m, t = 0.053 m	0.0009	h/D = 4 (h = 8 m)
Semi-rigid pile	D = 5 m, L = 25 m, t = 0.113 m	0.0305	h/D = 4 (h = 20 m)
Rigid pile	D = 10 m, L = 25 m, t = 0.213 m	0.4606	h/D = 4 (h = 40 m)

hydraulically placed sand are 100% and 0.54, respectively, based on the ground investigation report. The water table at the time of the test program was at the depth of approximately 5.4 m, and the saturated bulk unit weight of the first soil layer above the water table is $\gamma_{sat} = 17.1$ kN/m^3 with $K_0 = 0.4$ assumed (Chow and Jardine, 1996; Zdravković et al., 2020).

2.2. 3D finite element model

The 3D numerical model is built by the software ABAQUS, and given the symmetry of the problem, only half of the ground and the pile is modeled to save the computational cost (Fig. 3). Considering the embedded depths of the test piles are not long enough to cause the soil plugging and the mobilized soil area by the lateral displacement of the pile was far beyond the influenced soil area due to pile installation (Ma et al., 2017; Taborda et al., 2020; Yang et al., 2021; Yu and Yang, 2012), the soil plugging phenomenon and pile installation effect are neglected in the present analysis and the length of the soil inside the pile is assumed to be equal to the penetration depth of the pile. The diameter and the height of the soil domain are set as around 80D and 6.5L (D is the pile diameter and L is the embedded depth of the pile), respectively, to eliminate the boundary effect in the analysis. Compared with the usually adopted size of (15–20)D and height=(1.67–3.3)L of the soil domain in the literature (Ahmed and Hawlader, 2016; Sun et al., 2020; Wang et al., 2020a), the size of the soil domain in the model is large enough.

As for the boundary conditions, the displacements in all coordinate directions at the base and that perpendicular to the vertical sides of soil domain are constrained. The displacement perpendicular to the symmetry plane of the pile is restricted while the rotational degrees of freedom about the X- and Z-axes of this plane are set to be zero, which allowed the rotation of the pile along the Y-axis under lateral loading. A reference point is established at the center of the pile top at which a concentrated force is applied, and the kinematic degrees of freedom along the perimeter at the pile top are coupled with this reference point at this reference point. The pile-soil interaction is modeled by the finite-
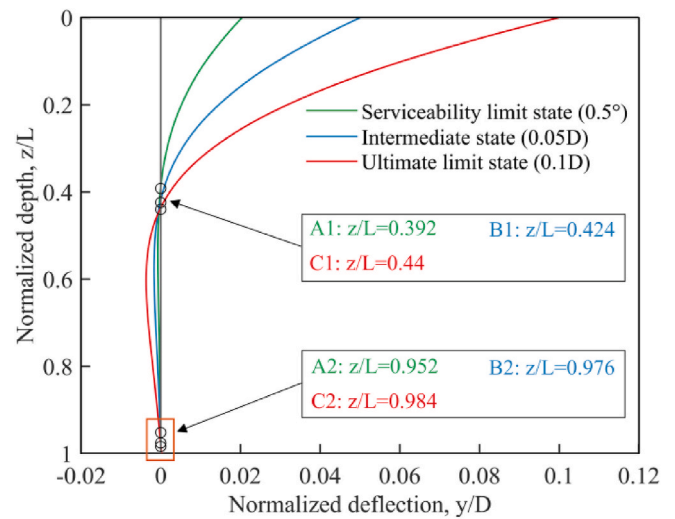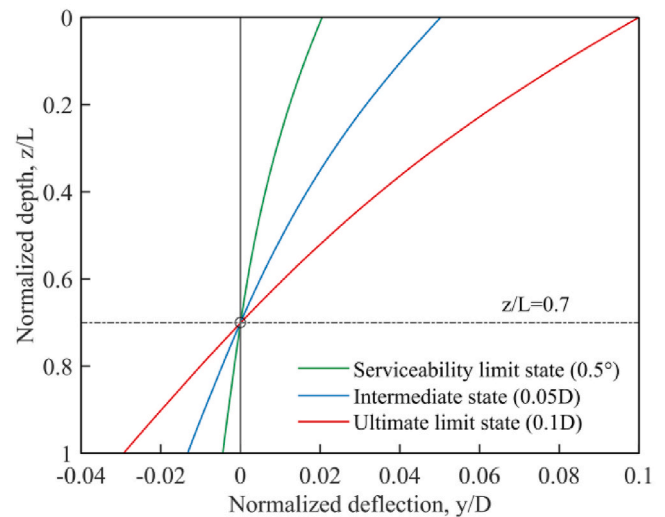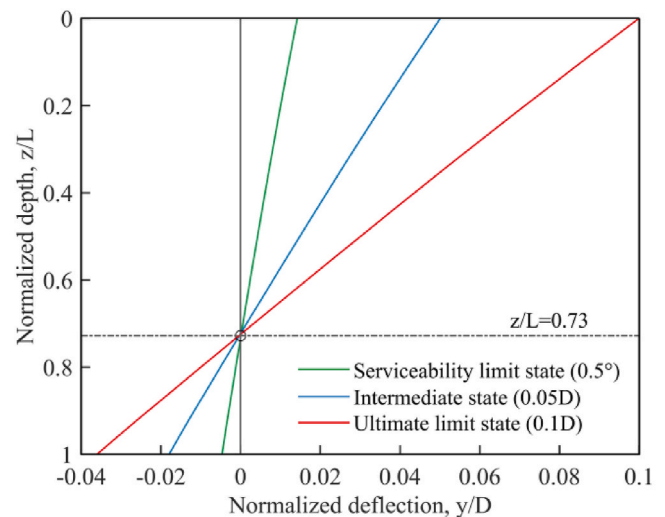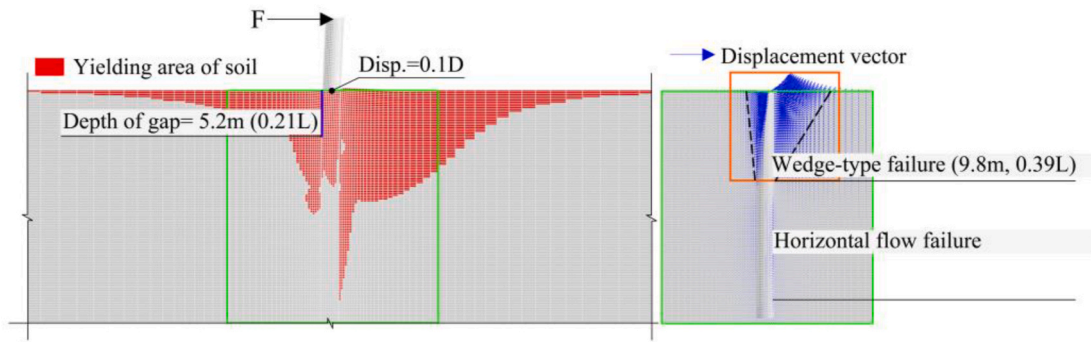

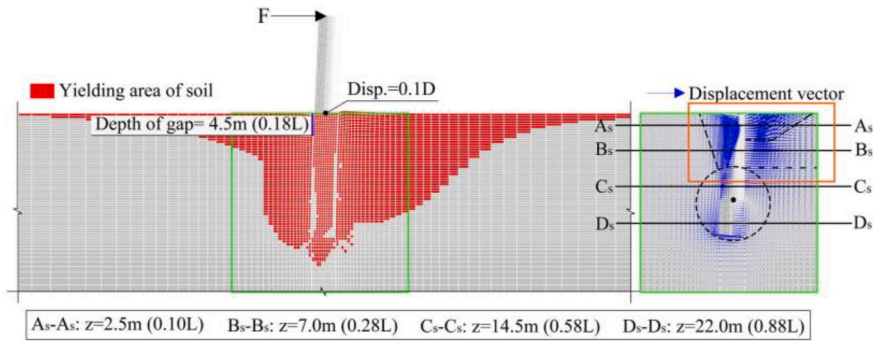**Fig. 7.** Deformation modes: (a) flexible pile; (b) semi-rigid pile; (c) rigid pile.

(a)

(b)

Fig. 8. Soil deformation mechanisms: (a) flexible pile; (b) semi-rigid pile; (c) rigid pile.

(c)
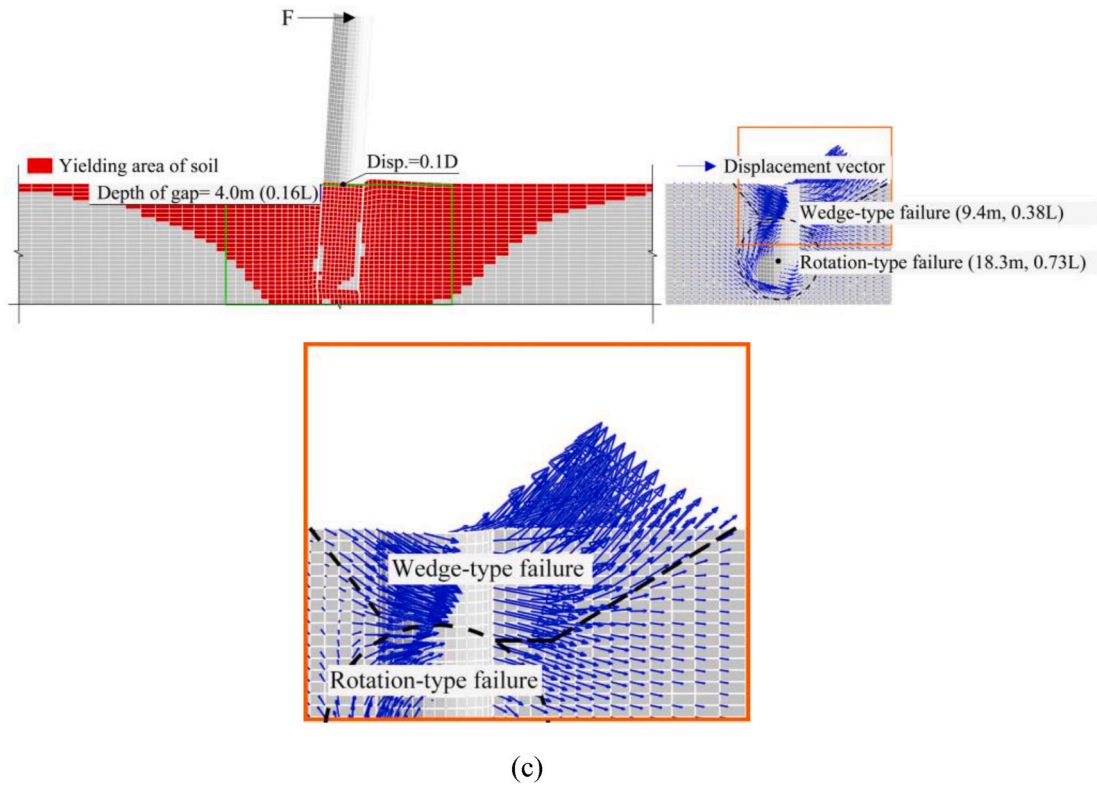
Fig. 8. (*continued*).
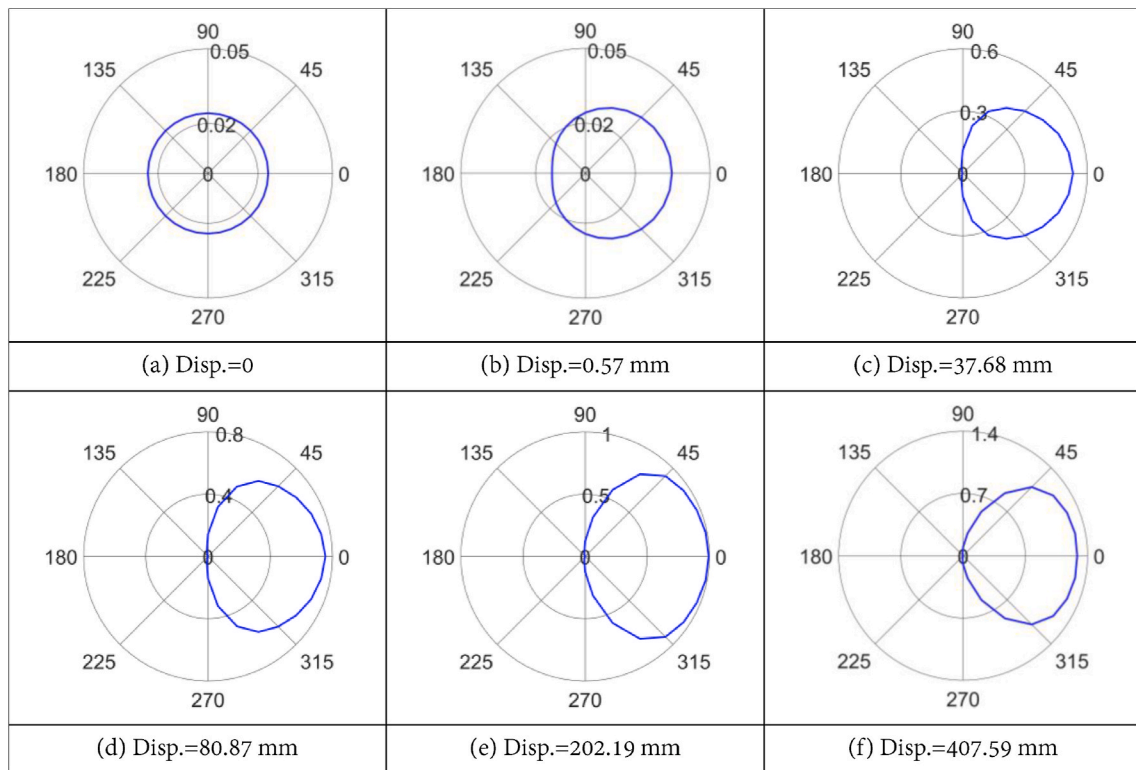
Fig. 9. Development of the earth pressure at A_s–A_s section (Unit: MPa).

sliding, surface-to-surface master/slave contact pair formulation between the outside, the inside, and the bottom surfaces of the pile and the contacted soil surfaces. The penalty method with a friction coefficient of 0.62, corresponding to the friction angle at the critical state obtained by the triaxial compression tests in the PISA project (Taborda et al., 2020), is adopted in the tangential direction of the contact pairs. The Lagrange
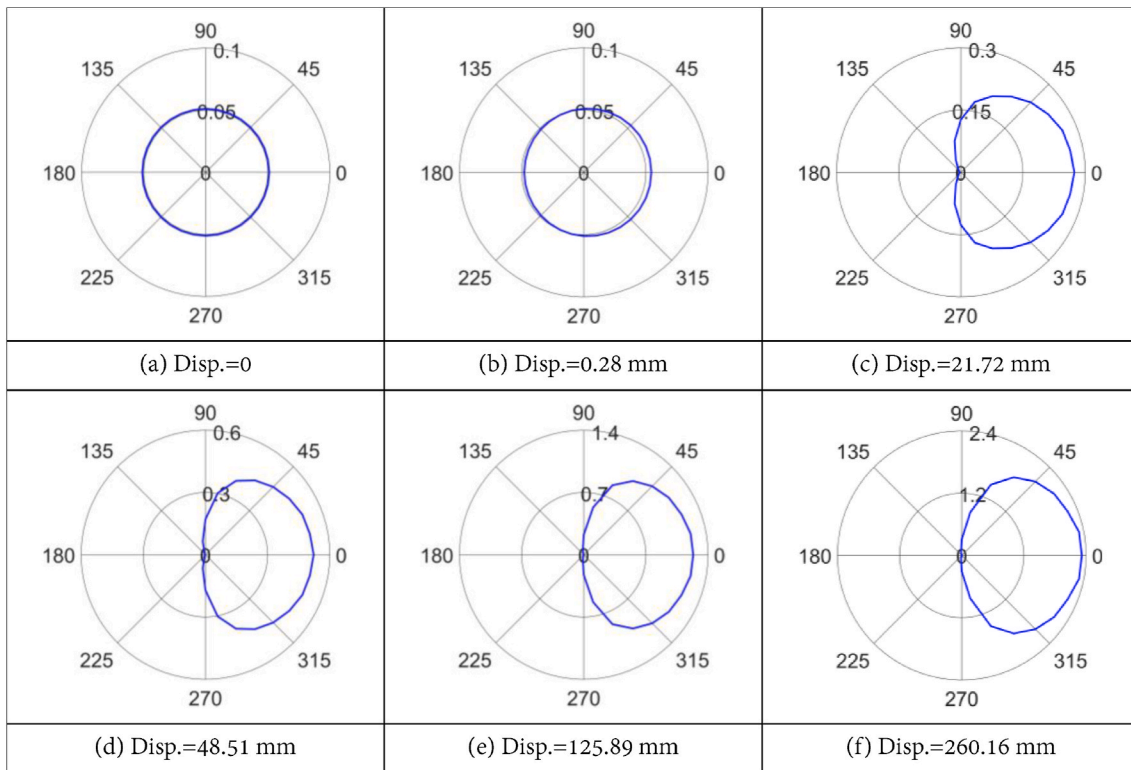
Fig. 10. Development of the earth pressure at B_s-B_s section (Unit: MPa).
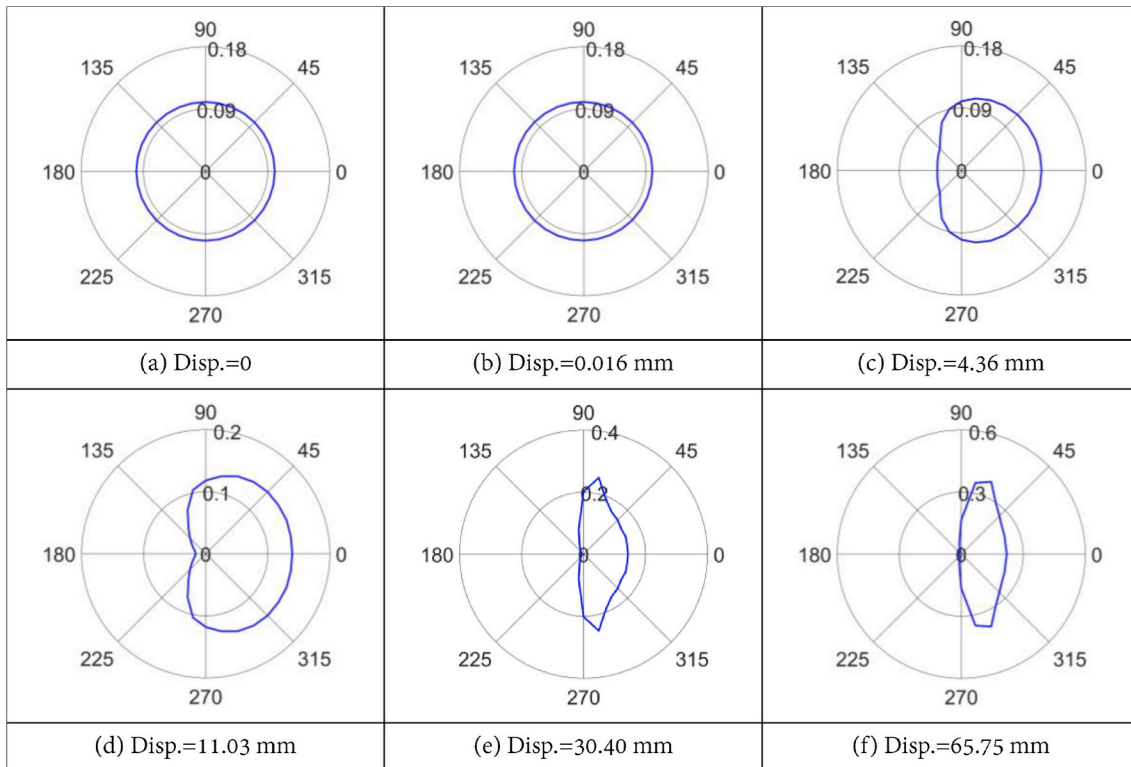
Fig. 11. Development of the earth pressure at C_s–C_s section (Unit: MPa).

multiplier method with an option to allow the separation is used in the normal direction of the contact pairs to model a possible gap between the pile and the soil during lateral loading (Ma et al., 2017).

In the FE models, the steel piles with the same geometric charac-teristics of DS1 and DM7 are discretized by 9630 and 6930 8-noded hexahedral solid elements, respectively. The reason for adopting solid elements rather than the shell elements to build the pile is that the solid element can effectively avoid the penetration problem associated with

(a) Disp.=0   (b) Disp.=-0.11 mm   (c) Disp.=-5.96 mm

(d) Disp.=-13.59 mm   (e) Disp.=-40.61 mm   (f) Disp.=-89.30 mm

Fig. 12. Development of the earth pressure at D_s-D_s section (Unit: MPa).

pile-soil interfaces during lateral loading. As shown in Fig. 4 (a), the soil elements behind the pile appear partially on the inner surface of the pile, meaning that the interface between the outer surface of the pile and the surrounding soil is not properly constructed. This may result in the occurrence of nonconvergence before the prescribed mudline displacement in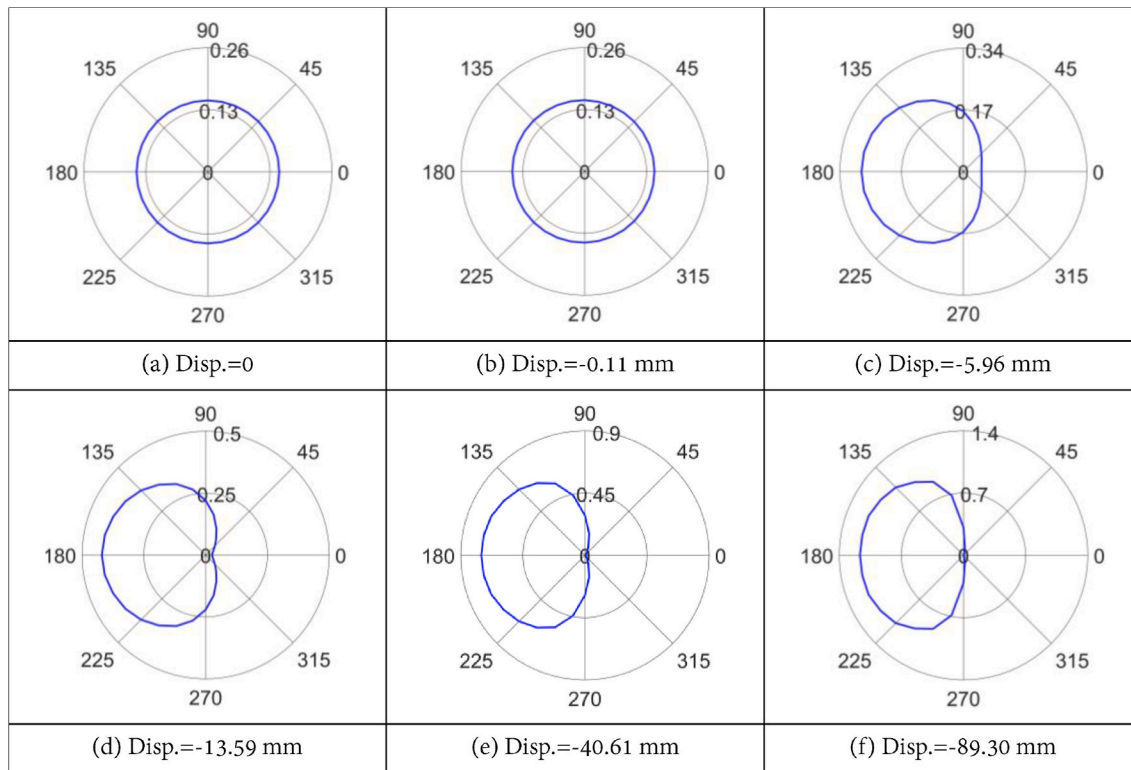 the numerical simulation. No such penetration problem occurs when the pile is built by the solid elements, as shown in Fig. 4 (b). The behavior of the steel pile is assumed to be linear elastic with Young's modulus, $E = 200\,\mathrm{GPa}$, the Poisson's ratio, $\upsilon = 0.30$, as well as the typical unit weight of steel, $\gamma_{st} = 78.5\,\mathrm{kN/m^3}$. The soil domains surrounding DS1 and DM7 are discretized by 63840 and 40550 8-noded hexahedral solid elements with reduced integration.

2.3. Parameter values for the Mohr-Coulomb model

Although the Mohr-Coulomb (MC) model can hardly reproduce the complex response of soil under cyclic loading, it is widely used in the industry due to its simplicity and acceptable accuracy in many geotechnical applications. As the present study is concerned with the soil-monopile interaction under monotonic lateral loading, the MC model is adopted. As shown later, a reasonable performance can be produced if the model parameters are properly determined by considering soil mechanics principles. For cyclic loading conditions, more advanced soil constitutive models, such as the Sanisand model (Dafalias and Manzari, 2004) or its evolved versions (Dafalias and Taiebat, 2016; Taborda et al., 2014; Wei et al., 2020) can be chosen; nevertheless, the difficulty and uncertainty in determining the large number of model parameters and in model implementation should not be overlooked.

The Poisson's ratio (υ) of the dense sand at Dunkirk is estimated to be 0.17 according to Kuwano (1999) while the Young's modulus (E) is estimated as 90 MPa for dense sand with relative density 90% according to Ahmed and Hawlader (2016). Note that the constant E value can be regarded as an average modulus over the depth of the sand deposit. Based on the triaxial compression tests for Dunkirk sand samples in PISA project (Zdravković et al., 2020), the peak friction angle is estimated to

be 42° from the relationship $M_p^c = q/p' = 6\,sin\,\varphi_p'/(3 - sin\,\varphi_p')$. This value is consistent with that recommended by API for dense sand (Ahmed and Hawlader, 2016), 41.5°. As for the dilatancy angle (ψ), it is estimated using the following relationship (Sharafutdinov et al., 2021):

$$sin\psi = I_R/(I_R + 6.7) \tag{1}$$

where $I_R = I_D(Q - lnp) - R$; Q and R are empirical coefficients, which for most soils can be taken as 10 and 1, respectively. Given the relative density I_D and mean effective stress, $\psi = 30°$ can be calculated. Similarly, $\psi = 29.1°$ and $\psi = 28.2°$ can also be calculated at the middle embedded depths of 0.70 m and 1.15 m for DS1 and DM7 by the following relationship of Yang and Li (2004):

$$\psi = -106.46\Psi_0 - 0.46 \tag{2}$$

where $\Psi_0 = e - e_c$ is the initial state parameter; $e_c = e_\Gamma - \lambda_c(p'/p_a)^\xi$ is the critical state curve in the $e - p'$ plane and e_Γ, λ_c and ξ are material constants, the values of which are reported by Zdravković et al. (2020). Based on the above discussion, $\psi = 30°$ is adopted in the MC model for the dense hydraulically placed sand. The parameters of the MC model in this study are summarized in Table 2.

2.4. Comparison of lateral load-displacement responses

The load-displacement curves of pile DS1 and pile DM7 predicted by the FE analysis, together with the filed test data are shown in Fig. 5, where y is calculated as the average of the pile leading and trailing edge displacement at the mudline, and $y = 0.1D$ is deemed as the displacement for the ultimate capacity, same as that in the PISA project. By the comparison, the simulation result of pile DM7 is in good agreement with the field test result, whereas the discrepancy between the simulation result of pile DS1 and the field test result is relatively large, as shown in Fig. 5. The reason for this discrepancy is that the embedded depth of pile DS1 is much shallow (L = 1.4 m) such that the overturning failure is more likely to occur. The overturning failure mode is often accompanied
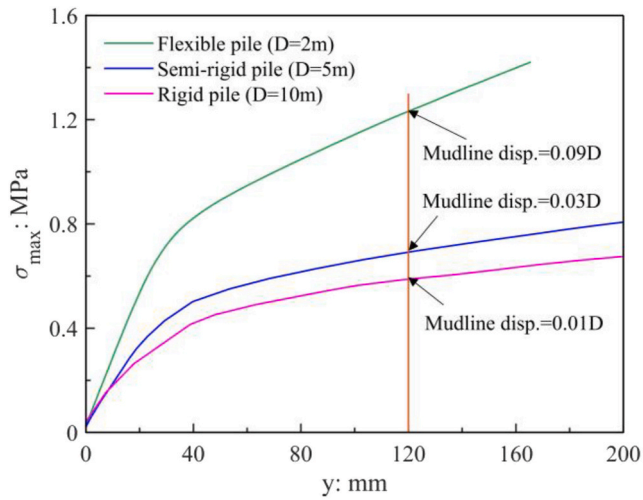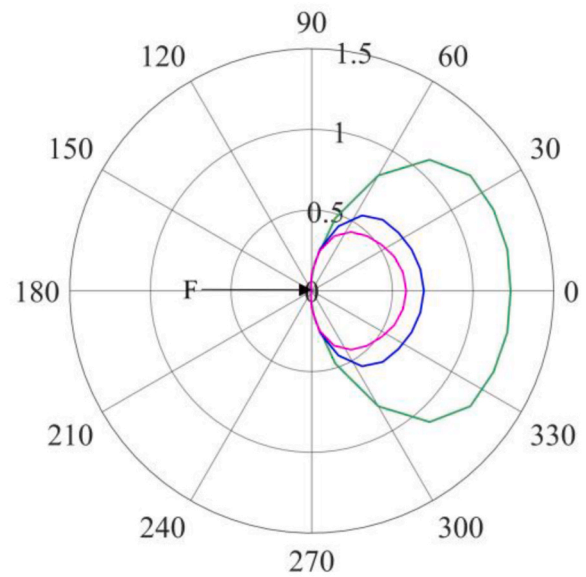
(a)
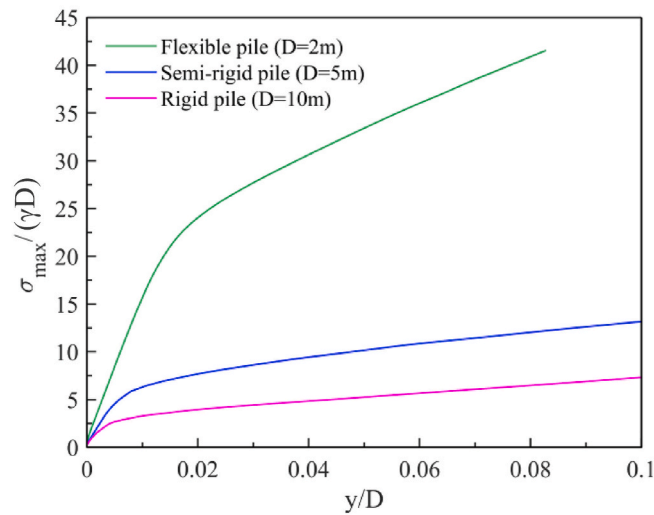
(b)

Fig. 13. Relationship between (a) maximum normal contact stress and section displacement and (b) normalized maximum normal contact stress and normalized displacement (depth = 2 m, z/L = 0.08).

by a more profound gap between pile and surrounding soil, which may result in the problem of singularity and non-convergence in the numerical simulation. In the PISA project, pile DS1 was principally used to check the bespoke loading and monitoring system on the site (Taborda et al., 2020), so the reliability of its field test result might be not as high as pile DM7.
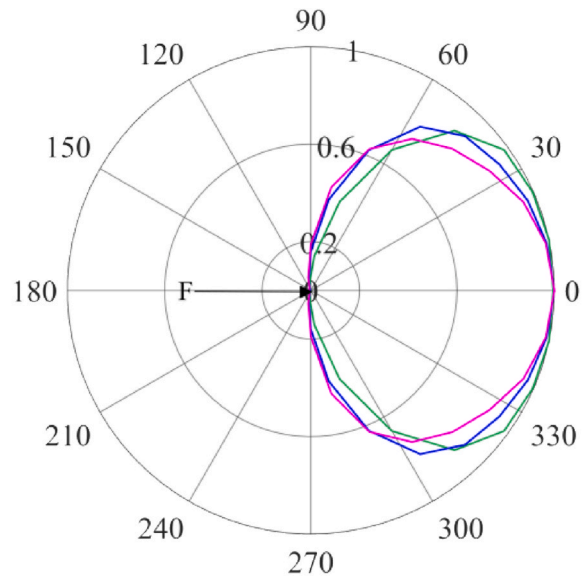
2.5. Comparison of the gap depth

In the field test, a gap between pile DM7 and the surrounding soil was observed on the back side of the pile and the depth of the gap was measured 1.15 m after the final unloading stage (McAdam et al., 2020), which corresponds to the mudline displacement of 0.073D (Fig. 5 (b)). In the numerical simulation of pile DM7, a gap of 1.11 m depth is observed when the mudline displacement arrives at 0.1D, as shown in Fig. 6, in which the gap on the pile-soil interface is mapped to the vertical plane passing through the pile center for the convenience of diagrammatic description. This value is in good agreement with the gap depth measured in the field test, suggesting that the 3D FE model can produce a reasonable prediction and the contact model adopted in the

Fig. 14. Comparison of normal contact stresses (in MPa) across pile perimeter (depth = 2 m and section displacement = 120 mm).

Fig. 15. Comparison of normalized normal contact stresses across pile perimeter (depth = 2 m and section displacement = 120 mm).

simulation can reproduce the gap development satisfactorily. This is important for accurate description of the earth pressure distribution and the associated soil deformation mechanism along the pile, as will be discussed in more detail in the next sections.

3. Pile slenderness effect on the distribution of earth pressure

Most of the recent studies on laterally loaded monopiles have tended to focus on the load-deflection response and the moment distribution (Hu et al., 2021; Li et al., 2017; Luo et al., 2020; Murphy et al., 2018; Taborda et al., 2020). The attention of the present study is placed on the
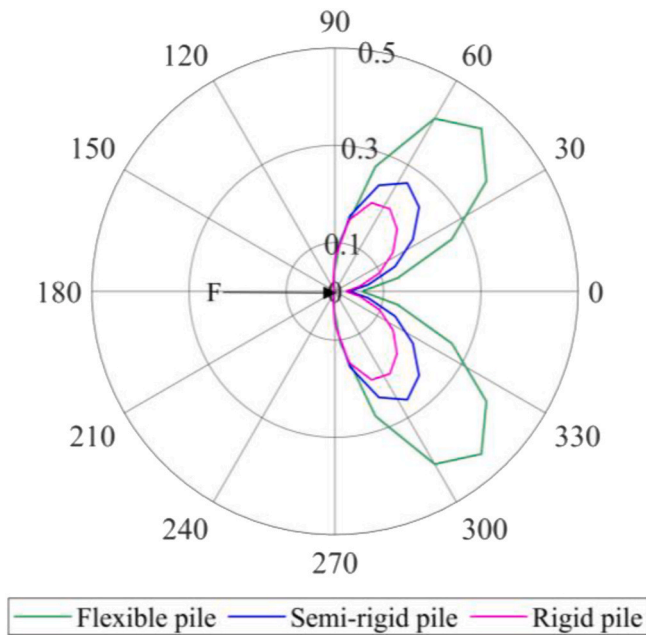
Fig. 16. Comparison of shear stresses (in MPa) across pile perimeter (depth = 2 m and section displacement = 120 mm).
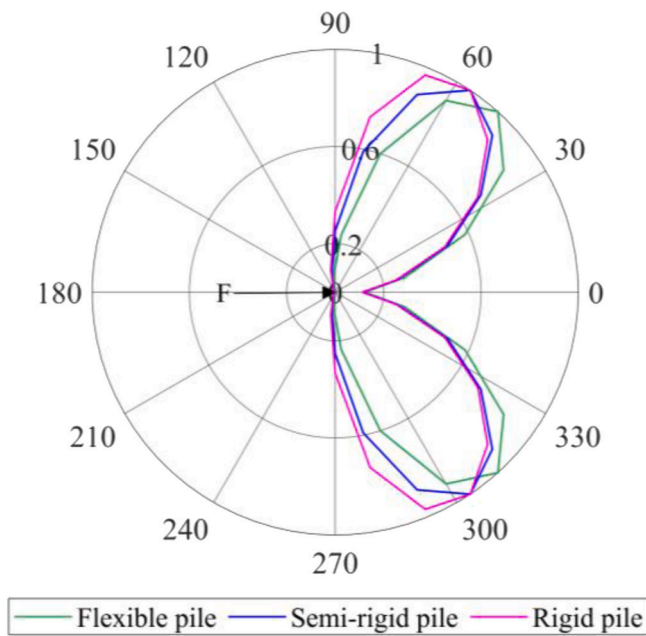

Fig. 17. Comparison of normalized shear stresses across pile perimeter (depth = 2 m and section displacement = 120 mm).

distribution of earth pressure and the deformation mechanism of the surrounding soil for monopiles with largely different diameters (2 m, 5 m and 10 m). To better understand the progressive development of earth pressure, three states during loading of the monopile are considered, including the serviceability limit state, i.e. 0.5° of the pile rotation at the mudline level (Det Norske Veritas, 2011), the ultimate limit state, i.e. 0.1D of the pile deflection at the mudline, and the intermediate state corresponding to pile deflection at the mudline level of 0.05D.

3.1. Criterion to characterize pile stiffness

For piles with different diameters, embedded depths and materials,

the index proposed by Poulos and Hull (1989), as given in equation (3), is useful to characterize pile stiffness:

$$S = \frac{E_p I_p}{E_s L^4} \tag{3}$$

where S is a dimensionless index to characterize pile stiffness; E_p and E_s are the elastic moduli of the pile and soil, respectively; L is the pile embedded depth; I_p is the moment of inertia of the pile.

Using this index, a pile can be classified as flexible, semi-rigid, or rigid: the upper bound for a flexible pile is 0.0025 and the lower bound for a rigid pile is 0.208, while a pile with S value between these two bounds is defined as the semi-rigid pile (Wang et al., 2020b). In the present study, the embedded depth and the load eccentricity ratio (i.e., the ratio of the height of the lateral load above the mudline to the pile diameter) are set as 25 m and 4, respectively. Therefore, the monopile with the diameter of 2 m is classified as a flexible pile, the monopile with the diameter of 10 m is a rigid pile, and the monopile with the diameter of 5 m is a semi-rigid pile. The wall thickness of the monopile is set as twice the minimum value ($t_{min} = 6.35 + D/100$, unit: mm) as recommended by the API standard (API, 2007); this wall thickness can efficiently avoid the buckling of the pile during loading. The detailed information of the simulated piles is summarized in Table 3, and the soil properties are the same as listed in Table 2.

3.2. Comparison of deformation modes

How pile deflection is affected by pile diameter is an important question as it informs the development of earth pressure on the pile. Shown in Fig. 7 are the deflection modes of the flexible pile (D = 2 m), the semi-rigid pile (D = 5 m) and the rigid pile (D = 10 m) at three different stages of loading. Clearly, the flexible pile exhibits flexural deflection whereas the rigid pile exhibits rotational deflection. The deflection mode of the semi-rigid pile is a kind of combination of these two modes. With the increase of lateral loading, the location of the upper rotation point of the flexible pile changes from 0.392L to 0.424L and then to 0.44L (L is the pile embedded depth from the mudline; the rotation points are denoted in sequence as A1, B1, and C1 in Fig. 7 (a)), accompanied by the reverse flexure with the lower rotation point changing from 0.952L to 0.976L and then to 0.984L (the rotation points are denoted in sequence as A2, B2 and C2 in Fig. 7 (a)). The major deflection of the flexible pile comes from the upper part of the pile. For the semi-rigid pile or the rigid pile, there is only one rotation point during the loading course and the point is fixed at 0.7L for the semi-rigid pile and at 0.73L for the rigid pile. In general, the rotation point tends to move downwards with the increase of pile stiffness (or pile diameter), along with the transformation from the flexural deflection to rotational deflection.

3.3. Comparison of soil deformation mechanisms

Fig. 8 shows the deformation patterns of the soils surrounding the flexible pile, the semi-rigid pile and the rigid pile. For the flexible pile, the wedge-type failure at shallow depth is clearly observed, Fig. 8(a), and this supports the assumption by Reese et al. (Reese et al., 1974); but the assumed horizontal flow failure at deep depth is not obvious in the simulation, due probably to the small lateral displacement of the flexible pile below the rotation point (refer to Fig. 7 (a)). This implies that the lateral bearing capacity of the flexible pile mostly comes from the wedge-type deformation of the soil at shallow depth. For the semi-rigid pile, a rotation-type deformation near the pile toe is observed along with the wedge-type failure and the horizontal flow above it, Fig. 8(b); this is corresponding to the combined flexural and rotational deflection of the semi-rigid pile as shown in Fig. 7. For the rigid pile, the soil flow mechanism is composed of the wedge-type failure and the rotation-type failure due to the rotational deflection of the rigid pile, Fig. 8 (c).
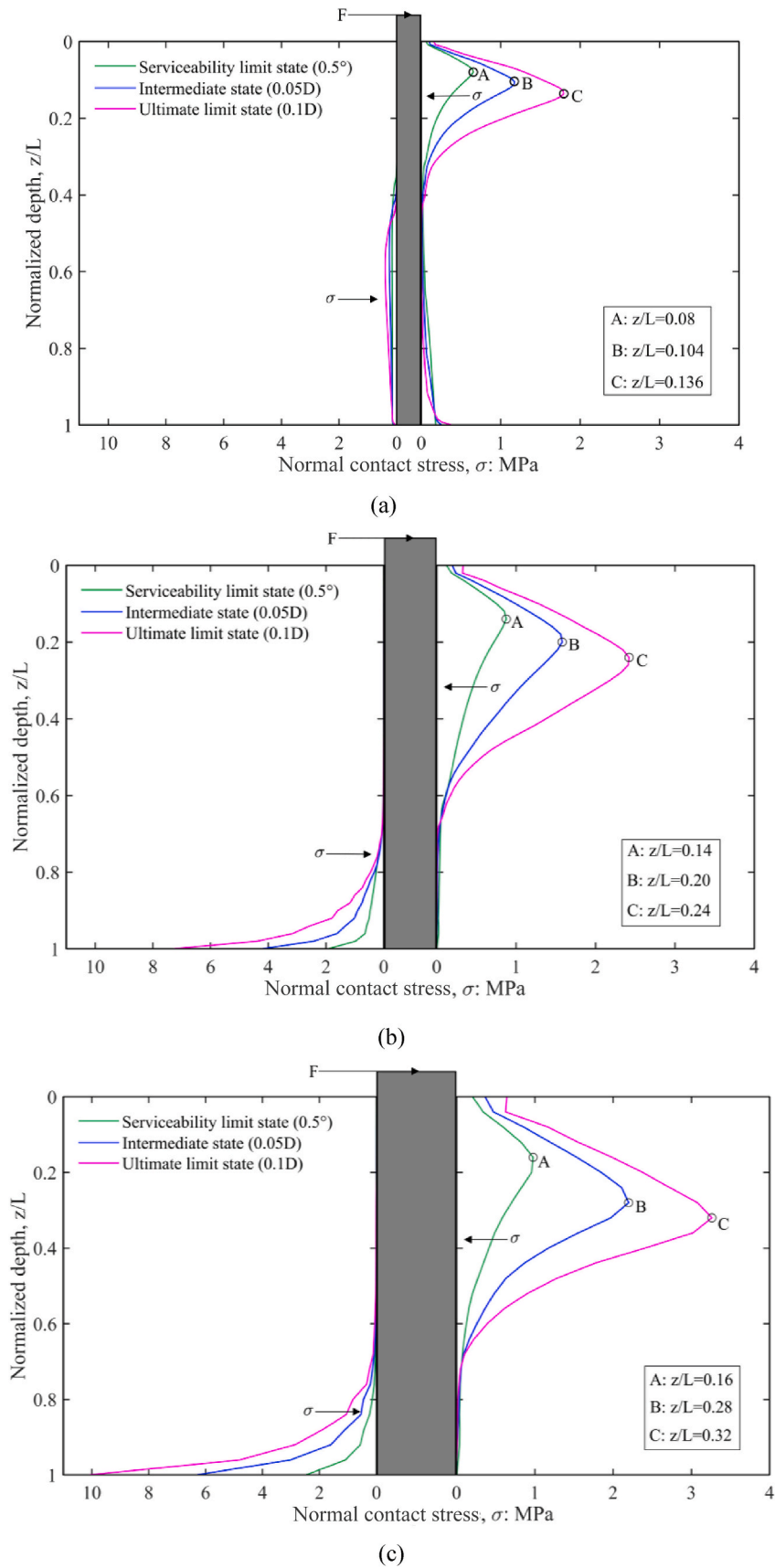
Fig. 18. Distribution of normal contact stresses: (a) flexible pile; (b) semi-rigid pile; (c) rigid pile.
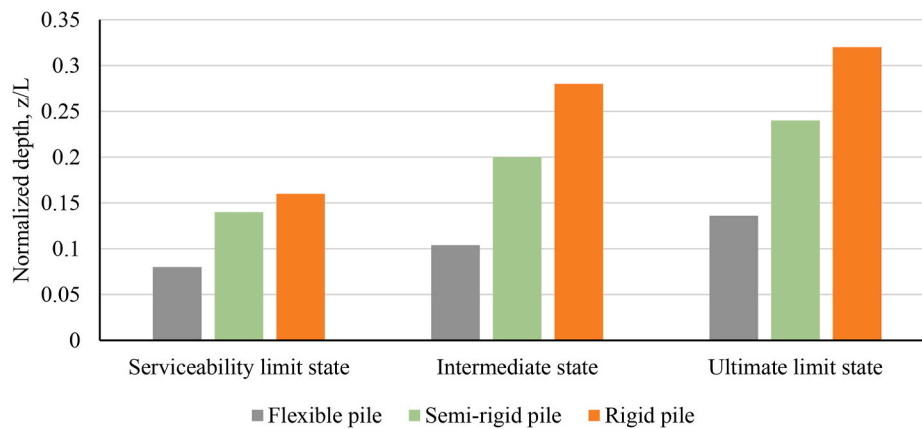
Fig. 19. Depth of the maximum normal contact stress on the front side of the pile.

3.4. Comparison of earth pressure across pile perimeter

Now, it is of interest to examine how earth pressure is mobilized along a monopile due to lateral loading. For limited space, only the results for selected sections A_s–A_s, B_s–B_s, C_s–C_s and D_s–D_s along the semi-rigid pile are discussed, since they represent all the three types of soil deformation modes described earlier. Fig. 9 shows the development of earth pressure at A_s–A_s section at different stages of loading in terms of mudline displacement, i.e. prior to loading, mudline displacement of 0.016%D, mudline displacement of 0.97%D, serviceability limit state (0.5° rotation), mudline displacement of 5%D, and the ultimate limit state (mudline displacement of 10%D). Similar results for other three sections are presented in Figs. 10–12. It is found that the active earth pressure behind a laterally loaded monopile becomes negligible after the mudline displacement reaches the serviceability limit state (0.5°) and the shape of the earth pressure distribution on the horizontal plane is like a vertical ellipse in the polar coordinates. It should be noted that the active earth pressure is mobilized in the opposite direction at section Ds-Ds, since it is located below the rotation point of the semirigid pile. Also, the section displacements are differing at these sections when the serviceability limit state is reached. For section Cs–Cs, the shape of earth pressure distribution tends to become angular after the serviceability limit state is exceeded; this is probably attributed to that the soil deformation mechanism at this depth is not only influenced by the rotation-type deformation but also by the horizontal flow pattern.

Fig. 13 presents a comparison of the relationship between maximum normal contact stress and the displacement of pile section at the depth of 2 m for the three cases of monopile diameter. It is clear that at a given displacement, the maximum normal contact stress becomes smaller with the increase of pile diameter. To make this point clearer, the distributions of normal contact stresses of the flexible pile, the semi-rigid pile and the rigid pile at the depth of 2 m and for the displacement of 120 mm are compared in Fig. 14. It is found that with the increase of pile diameter, the normal contact stress becomes smaller. This suggests that the extent of stress concentration for a large-diameter pile is less than that for a small-diameter pile. Therefore, the resistance from the surrounding soil in the unit area will become smaller with increasing pile diameter. The important implication is that if the p-y relationship is directly derived from the reduced-scale field test piles with small D and then applied to the design of large-diameter monopiles, the calculated bearing capacity will be overestimated. Therefore, a reduction coefficient should be introduced to allow for the pile slenderness effect.

On the other hand, when normalized by the maximum value, it is found that the distribution of the normal contact stress is nearly the same for all three cases of pile diameter and the shape is like a vertical ellipse in the polar coordinate (Fig. 15). The implication of this finding is that a unified factor independent of pile diameter can be introduced for averaging the contact normal stress across the pile section for simplified calculations.

For the same depth and the same displacement, the distributions of shear stress of the flexible pile, the semi-rigid pile and the rigid pile are compared in Fig. 16. It is found that for all three cases of pile diameter, the shape of shear stress distribution looks like a herringbone, with the maximum value approximately at $\theta = 60°$. The distribution is much different from that commonly assumed (Smith, 1987) where the maximum value appears at 90° (Fig. 2). This discrepancy can be explained by the Coulomb friction law. Note that the location of the maximum shear stress is influenced not only by the pile-soil relative slip but also by the upper limit determined by the Coulomb friction law; in this connection, its location cannot be at $\theta = 0$ where the pile-soil relative slip is zero, nor at $\theta = 90°$ where the normal contact stress is much small. The location of the maximum shear stress at approximately $\theta = 60°$ is thus considered reasonable. As far as the magnitude and the distribution of shear stress are concerned, similar conclusions as those for the normal contact stress can be drew, i.e., the stress magnitude is influenced by the pile diameter, while the distribution of the normalized stress is not (see Fig. 17).

3.5. Comparison of earth pressure along pile embedded depth

The results of normal contact stresses along the flexible pile, the semi-rigid pile and the rigid pile are shown in the three plots of Fig. 18. The maximum appears on the upper part of the flexible pile, whereas it occurs near the tip of the semi-rigid pile and the rigid pile. This difference is owing to the different soil deformation mechanisms as discussed before. That is, a wedge-type deformation of the soil will occur on the upper part of the flexible pile when subjected to lateral loading, while there will be not only a wedge-type deformation of the soil on the upper part but also a rotational deformation on the lower part for the semi-rigid pile and the rigid pile. Similar soil deformation modes were observed in the centrifuge test conducted by Hong et al. (2017). Moreover, with the increase of pile diameter or pile stiffness, the depth of the maximum normal contact stress on the front side of the pile becomes deeper, as shown in Fig. 19; this is because the depth of the mobilized soil increases when the deformation mode of the pile changes from the flexural to rotational deformation. On the other hand, for the semi-rigid pile or the rigid pile, the maximum normal contact stress on the rear side of the pile is much larger than that on the front side of the pile (3.02 times and 1.91 times for the semi-rigid pile and the rigid pile at the ultimate limit state, respectively). Therefore, local enhancement at the lower part may be needed for the semi-rigid pile and the rigid pile to avoid buckling of the pile body.

The results on the distribution of vertical shear stress along the pile are presented in Fig. 20. Similar features as those for contact normal stress are observed. The depth of the maximum vertical shear stress on the front side of the pile becomes deeper as the pile stiffness increases, as
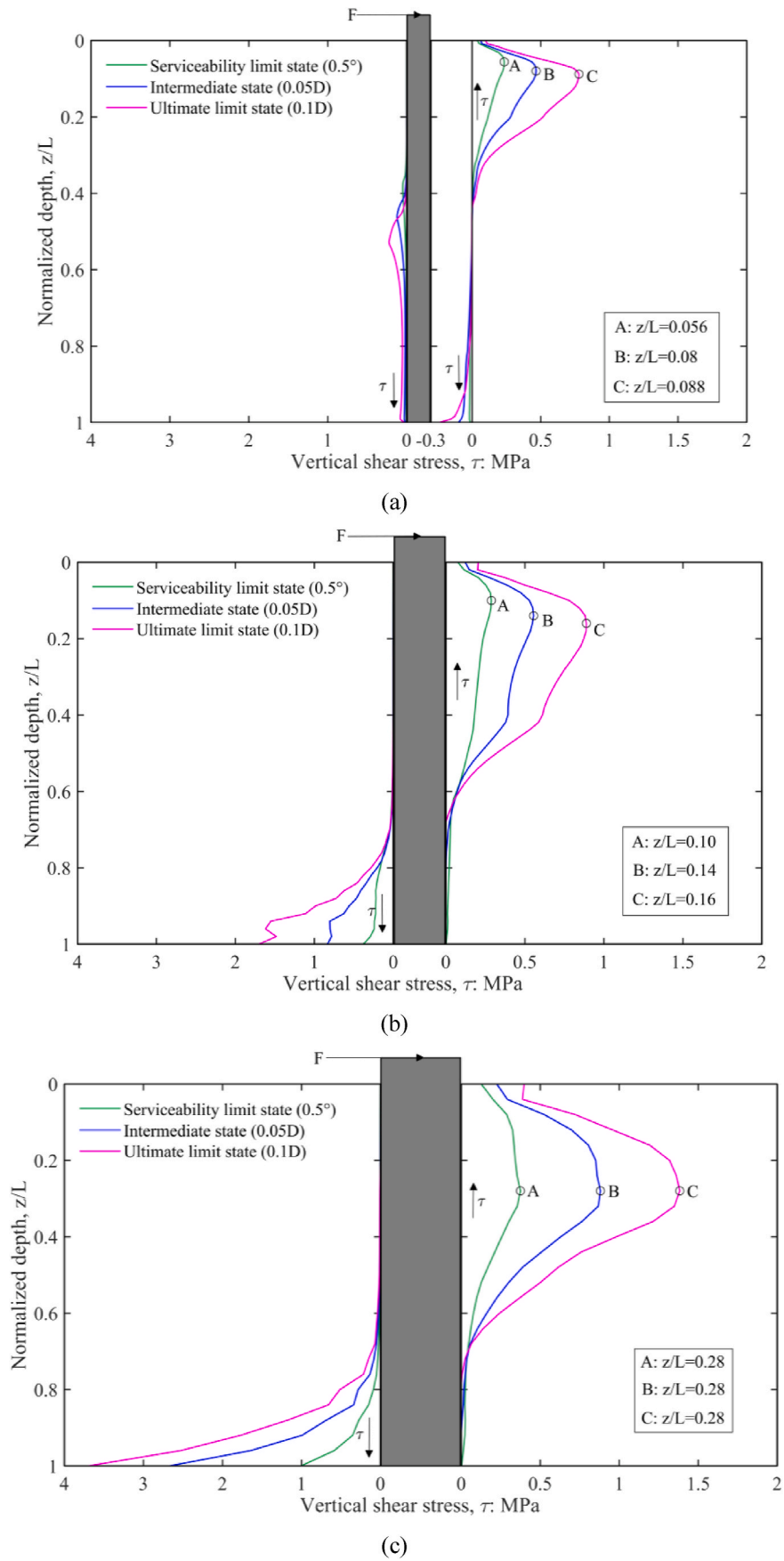
Fig. 20. Distribution of vertical shear stresses: (a) flexible pile; (b) semi-rigid pile; (c) rigid pile.
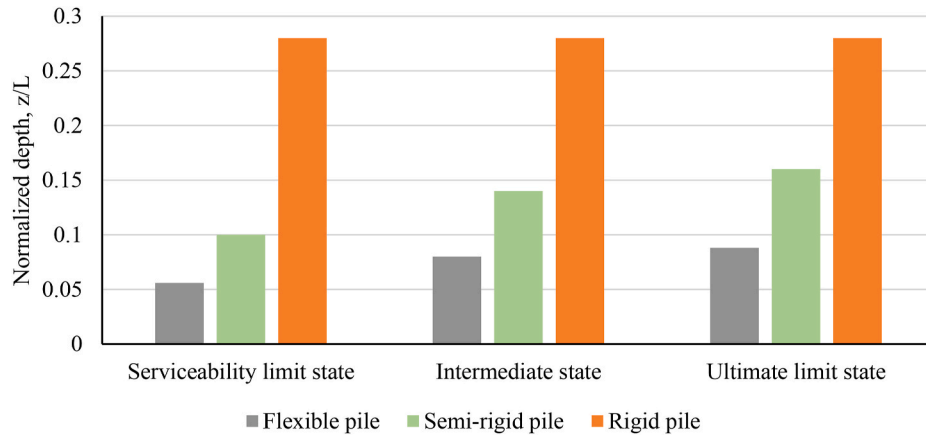
Fig. 21. Depth of the maximum vertical shear stress on the front side of the pile.
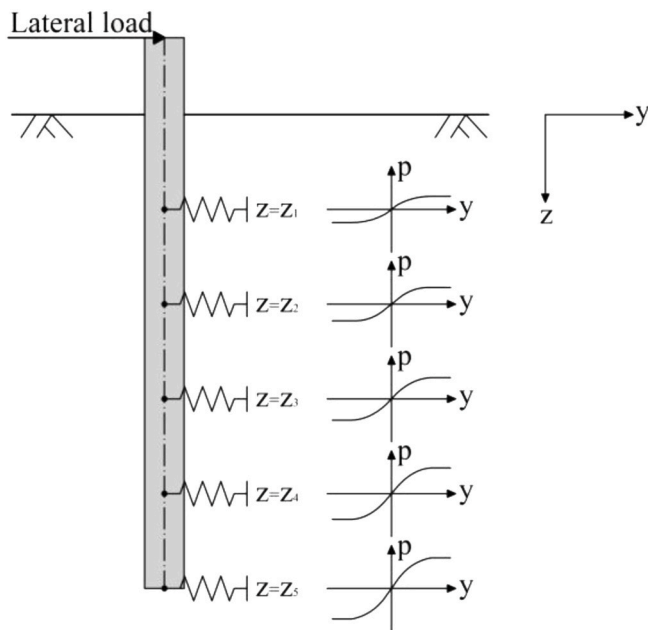

Fig. 22. Schematic of p-y curves.

shown in Fig. 21. For the case of rigid pile, the location of the maximum shear stress does not change when the pile loaded from the serviceability limit state to the ultimate limit state, but for the flexible pile the location tends to move downwards. This is because different deformation modes of the flexible pile and the rigid pile lead to different relative displacements between pile and soil and hence different magnitudes and distributions of shear stress.

4. Pile slenderness effect on the p-y relations

The p-y method is widely used in engineering practice to assess the bearing capacity of the laterally loaded pile due to its simplicity and efficiency. In this method, the pile-soil interaction problem is equivalent to a one-dimension beam supported by a serial of non-linear springs with the governing equation as follows:

$$EI \frac{d^4 y}{dz^4} - p = 0 \tag{4}$$

where, y is the lateral deflection of the pile at a given depth, z; E is the modulus of elasticity of the pile; I is the moment of inertia of pile section; p is the soil reaction per unit length.
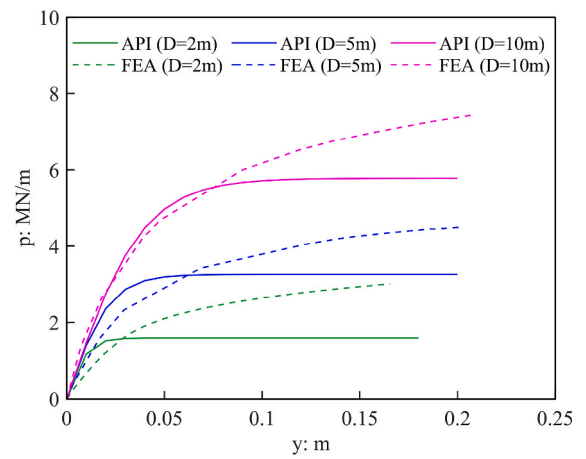
(a)
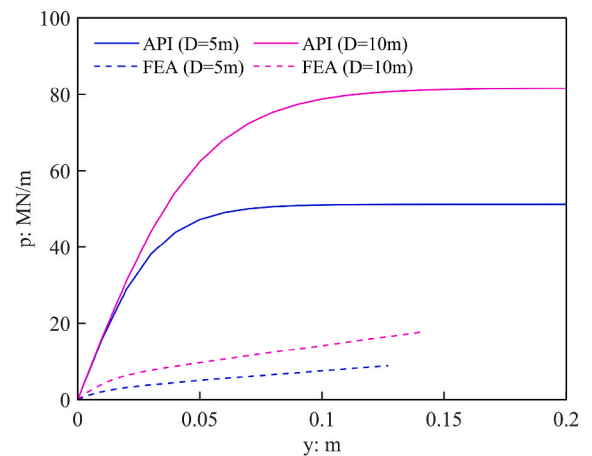
(b)

Fig. 23. Comparison of p-y curves for piles of different stiffness: (a) depth = 2 m (z/L = 0.08L); (b) depth = 22 m (z/L = 0.88L).

To solve the above differential equation, the relationships between p and y (i.e., a series of "p-y" curves or "p-y" springs, shown in Fig. 22) are required as input information; for example the p-y curves recommended in the API standard (API, 2007) are commonly employed.

4.1. API's recommendation

For the pile embedded in the sand, the tangent hyperbolic function in equation (5) is recommended to describe the relationship between the unit lateral soil resistance and pile deflection at depth of z:

$$p = A \times p_u \times \ \tanh\left(\frac{k \times z}{A \times p_u} \times y\right) \tag{5}$$

where A is a factor to account for cyclic or static loading condition and it is evaluated as $A = 0.9$ for cyclic loading or $A = (3.0 - 0.8H/D) \geq 0.9$ for static loading; p_u is the ultimate bearing capacity at depth z, which is the smallest value of equations (6) and (7); k is the initial modulus of subgrade reaction; the meanings of y and z are the same as those in equation (4).

$$p_{us} = (C_1 \times z + C_2 \times D) \times \gamma \times z \tag{6}$$

$$p_{ud} = C_3 \times D \times \gamma \times z \tag{7}$$

where γ is the effective soil weight; D is the average pile diameter from surface to depth; C_1, C_2 and C_3 are coefficients determined as function of φ' as follows:

$$C_1 = 0.115 \times 10^{0.0405\varphi'} \tag{8}$$

$$C_2 = 0.571 \times 10^{0.022\varphi'} \tag{9}$$

$$C_3 = 0.646 \times 10^{0.0555\varphi'} \tag{10}$$

Based on the field investigation report at Dunkirk (Zdravković et al., 2020), these coefficients can be determined as $C_1 = 5.78$, $C_2 = 4.79$, $C_3 = 138.43$ and $k = 74648 \ kN/m^3$.

4.2. Comparison of p-y curves for different stiffness piles

The p-y curves calculated using the formulas in API and derived from the 3D FE analyses are compared in Fig. 23 for the three cases of pile stiffness or pile diameter. Since the displacement of the flexible pile at the depth of 22 m (0.88L, L is the embedded depth) is negligible, the p-y curves are not compared at this depth.

At the depth of 2m (see Fig. 23 (a)), the initial stiffness of the p-y curve for the flexible pile (D = 2 m) and the semi-rigid pile (D = 5 m) is overestimated by the API method while the ultimate bearing capacity is underestimated compared with the results from the 3D FEM simulation. These observations are consistent with that reported in Klinkvort et al. (2010) and Wang et al. (2020a) and this discrepancy could be attributed to that very small diameter piles (D = 0.61 m) were used to derive the p-y curves in the API method (Reese et al., 1974). For the rigid pile (D = 10 m), the initial stiffness is slightly underestimated at the beginning by the API method, then the stiffness is overestimated with an underestimated ultimate bearing capacity. At the depth of 22 m (see Fig. 23 (b)), both the initial stiffness and the ultimate bearing capacity of the p-y curve are overestimated by the API method, which probably results from the different deformation modes for the semi-rigid pile and the rigid pile compared with the very small diameter piles used in the Mustang Island test (Reese et al., 1974). These discrepancies suggest that the pile slenderness effect on the p-y relation is complicated, depending on the location and the level of lateral displacement. Caution should be taken when using the p-y model established from field tests on small-diameter piles.

5. Conclusions

The rational design of large-diameter monopiles is a critical issue in the construction and operation of offshore wind turbines. Previous studies focused mainly on the deflection and moment of the laterally loaded pile itself. The attention of this study is placed on the effect of pile diameter on the distribution of earth pressure and the associated soil deformation mechanism. A good understanding of this effect plays an important role in the evaluation of the p-y models for large-diameter monopiles. A 3D finite element model has been built up and validated using quality field test data and then is applied to simulate three representative cases of monopiles (open-ended steel tubes with diameters of 2, 5 and 10 m, respectively, but with the same embedded depth of 25m). For each case, different loading stages are examined including the serviceability limit state, the ultimate limit state and the intermediate state. The main results and findings of this study are summarized as follows.

(a) As the pile diameter increases from 2 m to 10 m, the deflection mode of the pile varies from flexural deflection to rotational deflection and the deformation pattern of the surrounding soil, correspondingly, changes from the wedge-type to a combination of the wedge-type and the rotation-type. For all three cases of pile diameters, the active earth pressure behind the pile becomes negligible after the serviceability limit state (0.5°) is reached, and the earth pressure distribution on the horizontal plane looks like a vertical ellipse in the polar coordinates.

(b) At a given pile section and for a given section displacement, the magnitude of either normal contact stress or shear stress tends to decrease with increasing pile diameter. Accordingly, the resistance from the surrounding soil in a unit area will become smaller with increasing pile diameter. The important implication is that use of the p-y relationship derived from field tests on piles of reduced-scale in the design of large-diameter monopiles may still result in an overestimated lateral bearing capacity if the diameter of the test pile is small. A reduction factor should be introduced to allow for the pile slenderness effect.

(c) The shape of shear stress distribution looks like a herringbone, with the maximum value approximately at $\theta = 60°$ in the polar coordinates. This distribution is much different from that derived from the classical theoretical analysis that the maximum value appears at 90° (i.e. perpendicular to the lateral load direction). This discrepancy is mainly attributed to the assumption of the theoretical analysis that there is no relative slip or gap between the pile and the soil, and this assumption is considered inappropriate for real situations.

(d) When normalized by the maximum value, the distribution of the normal contact stress or the shear stress is nearly the same for all three cases of pile diameter. This finding suggests that a unified factor independent of pile diameter can be introduced to average the contact stress across the pile section in the development of simplified calculation methods.

Lastly, it should be mentioned that the soil type in the present study is dense sand, which is commonly encountered in the existing or planned offshore wind farms, and that the sand behavior is described using the Mohr-Coulomb model, which has its own advantages and limitations. Further studies of large diameter monopiles installed in various types of soils using more sophisticated constitutive models would be worthwhile.

CRediT authorship contribution statement

Yibo Ma: Methodology, Formal analysis, Writing – original draft. **Jun Yang:** Conceptualization, Methodology, Formal analysis, Supervision, Funding acquisition, Writing – review & editing.

Declaration of competing interest

The authors declare that they have no known competing financial interests or personal relationships that could have appeared to influence the work reported in this paper.

Data availability

Data will be made available on request.

Acknowledgment

References

Ahmed, S.S., Hawlader, B., 2016. Numerical analysis of large-diameter monopiles in dense sand supporting offshore wind turbines. Int. J. GeoMech. 16, 04016018 https://doi.org/10.1061/(asce)gm.1943-5622.0000633.

API, 2007. Recommended practice for planning, designing and constructing fixed offshore platforms, RP2A-WSD. Washington.

Baguelin, F., Frank, R., Said, Y.H., 1977. Theoretical study of lateral reaction mechanism of piles. Geotechnique 27, 405–434. https://doi.org/10.1680/geot.1977.27.3.405.

Bhushan, K., Lee, L.J., Grime, D.B., 1981. Lateral load tests on drilled piers in sand. ASCE. In: Drilled Piers and Caissons, pp. 114–131.

Breton, S.P., Moe, G., 2009. Status, plans and technologies for offshore wind turbines in Europe and North America. Renew. Energy 34, 646–654. https://doi.org/10.1016/j.renene.2008.05.040.

Burd, H.J., Taborda, D.M.G., Zdravković, L., Abadie, C.N., Byrne, B.W., Houlsby, G.T., Gavin, K.G., Igoe, D.J.P., Jardine, R.J., Martin, C.M., 2020. PISA design model for monopiles for offshore wind turbines: application to a marine sand. Geotechnique 70, 1048–1066.

Byrne, B.W., Houlsby, G.T., Burd, H.J., Gavin, K.G., Igoe, D.J.P., Jardine, R.J., Martin, C. M., McAdam, R.A., Potts, D.M., Taborda, D.M.G., 2020a. PISA design model for monopiles for offshore wind turbines: application to a stiff glacial clay till. Geotechnique 70, 1030–1047.

Byrne, B.W., McAdam, R.A., Burd, H.J., Beuckelaers, W.J.A.P., Gavin, K.G., Houlsby, G. T., Igoe, D.J.P., Jardine, R.J., Martin, C.M., Muir Wood, A., 2020b. Monotonic laterally loaded pile testing in a stiff glacial clay till at Cowden. Geotechnique 70, 970–985.

Cao, G., Ding, X., Yin, Z., Zhou, H., Zhou, P., 2021. A new soil reaction model for large-diameter monopiles in clay. Comput. Geotech. 137, 104311 https://doi.org/10.1016/j.compgeo.2021.104311.

Chen, L., Jiang, C., Pang, L., Liu, P., 2021. Lateral soil resistance of rigid pile in cohesionless soil on slope. Comput. Geotech. 135, 104163 https://doi.org/10.1016/j.compgeo.2021.104163.

Chow, F., Jardine, R.J., 1996. Investigations into the behaviour of displacement piles for offshore foundations. In: International Journal of Rock Mechanics and Mining Sciences and Geomechanics Abstracts. 319A–320A.

Cuéllar, V.P., 2011. Pile foundations for offshore wind turbines : numerical and experimental investigations on the behaviour under short- term and long-term cyclic loading. PhD Thesis, von der Fakultät VI - Planen Bauen Umwelt der Technischen Universität Berlin.

Dafalias, Y.F., Manzari, M.T., 2004. Simple plasticity sand model accounting for fabric change effects. J. Eng. Mech. 130, 622–634. https://doi.org/10.1061/(asce)0733-9399 (2004)130:6(622).

Dafalias, Y.F., Taiebat, M., 2016. Sanisand-Z: zero elastic range sand plasticity model. Geotechnique 66, 999–1013. https://doi.org/10.1680/jgeot.15.P.271.

(Det Norske Veritas), DNV, 2011. Offshore standard: design of offshore wind turbine structures. DNV-OS-J101. Høvik, Norway. DNV.

Hong, Y., He, B., Wang, L.Z., Wang, Z., Ng, C.W.W., Mašín, D., 2017. Cyclic lateral response and failure mechanisms of semi-rigid pile in soft clay: centrifuge tests and numerical modelling. Can. Geotech. J 54, 806–824. https://doi.org/10.1139/cgj-2016-0356.

Hu, Q., Han, F., Prezzi, M., Salgado, R., 2021. Finite-element analysis of the lateral load response of monopiles in layered sand. J. Geotech. Geoenviron. Eng. 148, 1–15. https://doi.org/10.1061/(ASCE)GT.1943-5606.0002745.

Klinkvort, R.T., Leth, C.T., Hededal, O., 2010. Centrifuge modelling of a laterally cyclic loaded pile. Phys. Model. Geotech. - proc. 7th Int. Conf, 2010, ICPMG 2010 Phys. Model. Geotech. 2, 959–964. https://doi.org/10.1201/b10554-158.

Kuwano, R., 1999. The stiffness and yielding anisotropy of sand. Ph. D. Thesis, Imperial College, University of London.

LeBlanc, C., Houlsby, G.T., Byrne, B.W., 2010. Response of stiff piles in sand to long-term cyclic lateral loading. Geotechnique 60, 79–90. https://doi.org/10.1680/geot.7.00196.

Lesny, K., Wiemann, J., 2006. Finite-element-modelling of large diameter monopiles for offshore wind energy converters. In: GeoCongress 2006: Geotechnical Engineering in the Information Technology Age, pp. 1–6.

Leung, D.Y.C., Yang, Y., 2012. Wind energy development and its environmental impact: a review. Renew. Sustain. Energy Rev. 16, 1031–1039. https://doi.org/10.1016/j.rser.2011.09.024.

Li, W., Zhu, B., Yang, M., 2017. Static response of monopile to lateral load in overconsolidated dense sand. J. Geotech. Geoenviron. Eng. 143, 04017026 https://doi.org/10.1061/(asce)gt.1943-5606.0001698.

Luo, R., Yang, M., Li, W., 2020. Numerical study of diameter effect on accumulated deformation of laterally loaded monopiles in sand. Eur. J. Environ. Civ. Eng. 24, 2440–2452. https://doi.org/10.1080/19648189.2018.1506828.

Ma, H., Yang, J., Chen, L., 2017. Numerical analysis of the long-term performance of offshore wind turbines supported by monopiles. Ocean Eng. 136, 94–105. https://doi.org/10.1016/j.oceaneng.2017.03.019.

McAdam, R.A., Byrne, B.W., Houlsby, G.T., Beuckelaers, W.J.A.P., Burd, H.J., Gavin, K. G., Igoe, D.J.P., Jardine, R.J., Martin, C.M., Muir Wood, A., 2020. Monotonic laterally loaded pile testing in a dense marine sand at Dunkirk. Geotechnique 70, 986–998.

Murphy, G., Igoe, D., Doherty, P., Gavin, K., 2018. 3D FEM approach for laterally loaded monopile design. Comput. Geotech. 100, 76–83. https://doi.org/10.1016/j.compgeo.2018.03.013.

O'Neill, M.W., Murchison, J.M., 1983. An evaluation of p-y relationships in sands. Research Rep. No. GT-DF02-83. University of Houston.

Poulos, H.G., Hull, T.S., 1989. The role of analytical geomechanics in foundation engineering. ASCE. In: Foundation Engineering: Current Principles and Practices, pp. 1578–1606.

Sharafutdinov, R.F., Isaev, O.N., Morozov, V.S., 2021. Experimental studies of cohesionless subsoil dilatancy under conditions of triaxial compression. Soil Mech. Found. Eng. 57, 465–472. https://doi.org/10.1007/s11204-021-09694-3.

Smith, T.D., 1987. Pile horizontal soil modulus values. J. Geotech. Eng. 113, 1040–1044. https://doi.org/10.1061/(ASCE)0733-9410(1987)113:9(1040).

Sun, Y., Xu, C., Du, X., El Naggar, M.H., Zhang, X., Jia, J., 2020. Nonlinear lateral response of offshore large-diameter monopile in sand. Ocean Eng. 216, 108013 https://doi.org/10.1016/j.oceaneng.2020.108013.

Taborda, D.M.G., Zdravković, L., Kontoe, S., Potts, D.M., 2014. Computational study on the modification of a bounding surface plasticity model for sands. Comput. Geotech. 59, 145–160. https://doi.org/10.1016/j.compgeo.2014.03.005.

Taborda, D.M.G., Zdravković, L., Potts, D.M., Burd, H.J., Byrne, B.W., Gavin, K.G., Houlsby, G.T., Jardine, R.J., Liu, T., Martin, C.M., 2020. Finite-element modelling of laterally loaded piles in a dense marine sand at Dunkirk. Geotechnique 70, 1014–1029.

Wang, H., Wang, L., Hong, Y., Askarinejad, A., He, B., Pan, H., 2021. Influence of pile diameter and aspect ratio on the lateral response of monopiles in sand with different relative densties. J. Mar. Sci. Eng. 9 https://doi.org/10.3390/jmse9060618.

Wang, H., Wang, L.Z., Hong, Y., He, B., Zhu, R.H., 2020a. Quantifying the influence of pile diameter on the load transfer curves of laterally loaded monopile in sand. Appl. Ocean Res. 101 https://doi.org/10.1016/j.apor.2020.102196.

Wang, L., Lai, Y., Hong, Y., Mašín, D., 2020b. A unified lateral soil reaction model for monopiles in soft clay considering various length-to-diameter (L/D) ratios. Ocean Eng. 212 https://doi.org/10.1016/j.oceaneng.2020.107492.

Wei, X., Chen, Y., Yang, J., 2020. A unified critical state constitutive model for cyclic behavior of silty sands. Comput. Geotech. 127, 103706 https://doi.org/10.1016/j.compgeo.2020.103760.

Yang, J., Li, X.S., 2004. State-dependent strength of sands from the perspective of unified modeling. J. Geotech. Geoenviron. Eng. 130, 186–198. https://doi.org/10.1061/(asce)1090-0241(2004)130:2(186).

Wind Europe, 2021. Offshore wind in Europe - key trends and statistics 2020. Wind Europe, Brussels, Belgium.

Yang, S., Deng, X., Yang, J., 2021. Modeling of soil-pile-structure interaction for dynamic response of standalone wind turbines. Renew. Energy 186, 394–410. https://doi.org/10.1016/j.renene.2021.12.066.

Yu, F., Yang, J., 2012. Base capacity of open-ended steel pipe piles in sand. J. Geotech. Geoenviron. Eng. 138, 1116–1128. https://doi.org/10.1061/(asce)gt.1943-5606.0000667.

Zdravković, L., Jardine, R.J., Taborda, D.M.G., Abadias, D., Burd, H.J., Byrne, B.W., Gavin, K.G., Houlsby, G.T., Igoe, D.J.P., Liu, T., 2020. Ground characterisation for PISA pile testing and analysis. Geotechnique 70, 945–960.

Zhang, L., Silva, F., Grismala, R., 2005. Ultimate lateral resistance to piles in cohesionless soils. J. Geotech. Geoenviron. Eng. 131, 78–83. https://doi.org/10.1061/(asce)1090-0241(2005)131:1(78).

Zhang, Y., Andersen, K.H., 2019. Soil reaction curves for monopiles in clay. Mar. Struct. 65, 94–113. https://doi.org/10.1016/j.marstruc.2018.12.009.

Zhu, B., Sun, Y.X., Chen, R.P., Guo, W.D., Yang, Y.Y., 2015. Experimental and analytical models of laterally loaded rigid monopiles with hardening p–y curves. J. Waterw. Port, Coast. Ocean Eng. 141, 04015007 https://doi.org/10.1061/(asce)ww.1943-5460.0000310.

Reese, L.C., Cox, W.R., Koop, F.D. 1974. Analysis of laterally loaded piles in Sand. Proceedings of the 5th annual offshore technology conference, Houston, TX, USA, vol. II, paper no. OTC 2080, 473-485.